AIAA JOURNAL
Vol. 39, No. 12, December 2001

Large-Eddy Simulation of Supersonic Compression-Ramp Flow by High-Order Method

Donald P. Rizzetta,* Miguel R. Visbal,† and Datta V. Gaitonde*
U.S. Air Force Research Laboratory, Wright–Patterson Air Force Base, Ohio 45433-7521

A high-order method is used to perform large-eddy simulations of a supersonic compression-ramp flowfield. The procedure employs an implicit approximately factored finite difference algorithm, which is used in conjunction with a 10th-order nondispersive filter. Spatial derivatives are approximated by a sixth-order compact scheme, and Newton-like subiterations are applied to achieve second-order temporal accuracy. In the region of strong shock waves, the compact differencing of convective fluxes is replaced locally by an upwind-biased scheme. Both the Smagorinsky and dynamic subgrid-scale stress models are incorporated in the simulations. Details of the method are summarized, and a number of computations are carried out. Comparisons are made between the respective solutions as well as with available experimental data and with previous numerical results.

Nomenclature

E = total specific energy
E_k = normalized spanwise turbulent kinetic energy spectra
$\boldsymbol{F}, \boldsymbol{G}, \boldsymbol{H}$ = inviscid vector fluxes
$\boldsymbol{F}_v, \boldsymbol{G}_v, \boldsymbol{H}_v$ = viscous vector fluxes
J = Jacobian of coordinate transformation
k_3 = nondimensional wave number in z direction
L_x, L_y, L_z = nondimensional domain extents
l_r = reference length
M_r = reference Mach number
Pr = Prandtl number; 0.73 for air
Pr_t = turbulent Prandtl number
p = nondimensional static pressure
$\boldsymbol{Q}$ = vector of dependent variables
$\boldsymbol{q}_i$ = components of heat flux vector
Re = reference Reynolds number, $\rho_r u_r l_r / \mu_r$
Re_θ = momentum thickness Reynolds number
$\mathcal{S}_{ij}$ = rate-of-strain tensor
$\mathcal{S}_M$ = magnitude of the rate-of-strain tensor
T = nondimensional static temperature
t = nondimensional time
U, V, W = contravariant velocity components
u, v, w = nondimensional Cartesian velocity components in x, y, and z directions
u_r = reference velocity
u_τ = friction velocity
u_1, u_2, u_3 = u, v, w
u^+ = u/u_τ
x, y, z = nondimensional Cartesian coordinates
x_1, x_2, x_3 = x, y, z
γ = specific heat ratio; 1.4 for air
Δ = eddy-viscosity length, grid-filter width
$\Delta \boldsymbol{Q}$ = $\boldsymbol{Q}^{p+1} - \boldsymbol{Q}^p$
Δt = time step size
$\Delta x, \Delta y, \Delta z$ = mesh step sizes
$\hat{\Delta}/\Delta$ = test-filter width to grid-filter width ratio
δ = nondimensional boundary-layer thickness
δ_{ij} = Kronecker delta function
$\delta_{\xi 2}, \delta_{\eta 2}, \delta_{\zeta 2}, \delta_{\xi 6}, \delta_{\eta 6}, \delta_{\zeta 6}$ = second- and sixth-order finite-difference operators in ξ, η, and ζ directions
δ^* = nondimensional boundary-layer displacement thickness
θ = nondimensional boundary-layer momentum thickness
μ = nondimensional molecular-viscosity coefficient
μ_t = nondimensional eddy-viscosity coefficient
ξ, η, ζ = computational coordinates
$\xi_t, \xi_x, \xi_y, \xi_z, \eta_t, \eta_x, \eta_y, \eta_z, \zeta_t, \zeta_x, \zeta_y, \zeta_z$ = metric coefficients of the coordinate transformation
ρ = nondimensional fluid density
Ω_z = nondimensional component of vorticity in z direction

Subscripts

i = inviscid value
m = time-mean value
r = dimensional reference value
vD = van Driest component
w = evaluated at the wall
0 = evaluated at the inflow location
1 = evaluated upstream of interaction

Superscripts

n = time level
p = subiteration level
$\bar{}$ = large-scale component
$\tilde{}$ = Favre-averaged component
$\hat{}$ = test-filtered component
$'$ = fluctuating component
$+$ = value given in law-of-the-wall units

Introduction

DIRECT numerical simulation (DNS) is characterized by severe resolution requirements of flows at high Reynolds numbers, especially near wall-bounded regions. Advances in the speed and storage capacity of computing machinery, however, have made it possible to perform DNS for a restricted class of turbulent flowfields. Although currently limited to relatively low Reynolds numbers and to simple geometric configurations, such computations can be extended through the use of large-eddy simulation (LES). This is accomplished in LES by leaving small-scale fluid structures spatially underresolved and accounting for them by means of a subgrid-scale (SGS) turbulence model. Although DNS and LES have quite

---

Presented as Paper 2000-2408 at the AIAA Fluids 2000 Conference, Denver, CO, 19–22 June 2000; received 26 July 2000; revision received 22 June 2001; accepted for publication 4 July 2001. This material is declared a work of the U.S. Government and is not subject to copyright protection in the United States. Copies of this paper may be made for personal or internal use, on condition that the copier pay the $10.00 per-copy fee to the Copyright Clearance Center, Inc., 222 Rosewood Drive, Danvers, MA 01923; include the code 0001-1452/01 $10.00 in correspondence with the CCC.

*Senior Research Aerospace Engineer, Computational Sciences Branch, Aeronautical Sciences Division. Associate Fellow AIAA.

†Technical Area Leader, Computational Sciences Branch, Aeronautical Sciences Division. Associate Fellow AIAA.

general applicability, until recently, the majority of flows considered by these methods have been incompressible or subsonic.

LES of supersonic flows are useful for studying compressibility effects, which can appreciably alter the fluid physics, including a substantial reduction in turbulence intensity levels.[1] Such studies increase the understanding of turbulence mechanisms and can lead to the development, improvement, and testing of lower-order closure models. Despite remaining computationally intensive, LES also may be beneficial for practical applications in the design and analysis of high-speed flight vehicles and associated propulsion systems where less sophisticated approaches fail.

One of the first significant direct supersonic simulations was that of Rai et al.[2] for a turbulent spatially evolving boundary-layer flow at a Mach number of 2.25 and $Re_\theta \approx 6 \times 10^3$. A corresponding LES of this same case was carried out by Spyropoulos and Blaisdell,[3] employing the dynamic subgrid stress model of Germano et al.[4] on coarser computational meshes. Both of these simulations utilized a fifth-order-accurate, upwind-biased finite difference description of inviscid fluxes, which was used in conjunction with a centered fourth-order-accurate approximation for viscous terms and were integrated in time by an implicit iterative technique.

The DNS of Lee et al.[5] and LES of Ducros et al.[6] have been used to study interactions of isotropic turbulence with a normal shock wave. Although the shock was relatively weak, simulations indicated that the increase in turbulence kinetic energy due to the interaction could not be predicted by linear theory.

Because of their geometric simplicity but fluid complexity, supersonic-compression ramp flowfields have been studied extensively, both experimentally and computationally. Andreopoulos and Muck[7] observed large-scale shock-wave oscillations at a frequency that was found to correlate with the bursting phenomenon of the upstream boundary layer. Smits and Muck[8] obtained detailed measurements of the fluctuating flowfield, which confirmed that observation. Experiments performed by Dolling and Murphy[9] at a Mach number of 3.0, however, detected shock-wave motion that was random. This result was verified by Dolling and Or,[10] who noted that incipient separation occurred for a ramp angle of 16 deg. A resolution of the apparent controversy over these observations was arrived at by Erengil and Dolling,[11,12] who concluded that the shock motion contains both large-scale and small-scale fluctuations. Whereas these oscillations are generally random, there is a correlation between the shock-wave motion and pressure fluctuations in the upstream boundary layer.

Computational investigations of supersonic compression-ramp flows have most often employed Reynolds-averaged equations in conjunction with mean turbulence models. Such efforts have met with limited success in the prediction of quantities such as heat transfer and skin friction, particularly for situations with large reversed-flow regions.[13] It is postulated that this difficulty may be due in part to the disparity between the time-mean and instantaneous shock-system structure. In addition, the models and resultant computations often fail to account for compressibility effects or the three dimensionality of the flowfield.

Hunt and Nixon[14] performed a very large-eddy simulation of a 24-deg compression ramp at Mach 2.8, which indicated a correlation between upstream fluctuations and shock-wave motion. For the Mach 3.0 flow past an 8-deg ramp, no separation was found in the LES of Urbin et al.[15] Some preliminary results were later obtained at a ramp angle of 25 deg (Ref. 16). Adams[17,18] carried out a DNS for an 18-deg compression ramp at Mach 3.0, which indicated a small region of reversed mean flow but no large-scale shock-wave motion.

The present effort considers LESs of supersonic compression-ramp flow by application of a time-implicit high-order compact finite difference scheme, which is used in conjunction with a 10th-order spatial filter. This technique previously has been used successfully by Rizzetta et al.[19] for subsonic LES of channel and cylinder flowfields. In regions of shock waves, the compact differencing of convective fluxes is replaced locally by an upwind-biased scheme. The governing equations are summarized, including a description of the SGS stress models, and details of the numerical procedure are presented. Computations are performed for the supersonic flow past a compression ramp. LES results are compared, along with available experimental data and with a previous existing computation.

Governing Equations

The governing equations are the unsteady three-dimensional compressible Favre-filtered Navier–Stokes equations, written in nondimensional variables and expressed notationally in the following conservative form:

$$\frac{\partial \boldsymbol{Q}}{\partial t} + \frac{\partial}{\partial \xi}\left(\boldsymbol{F} - \frac{1}{Re}\boldsymbol{F}_v\right) + \frac{\partial}{\partial \eta}\left(\boldsymbol{G} - \frac{1}{Re}\boldsymbol{G}_v\right) + \frac{\partial}{\partial \zeta}\left(\boldsymbol{H} - \frac{1}{Re}\boldsymbol{H}_v\right) = 0 \tag{1}$$

The filtered form of an arbitrary variable f is given by

$$\bar{f} = \int_{\mathcal{V}} \mathcal{G} f \, \mathrm{d}\mathcal{V} \tag{2}$$

where $\mathcal{G}$ is the grid filtering function and the integration is carried out over the entire flow domain. This allows f to be decomposed into its large-scale, $\bar{f}$, and subgrid-scale, f_{sg}, components

$$f = \bar{f} + f_{\text{sg}} \tag{3}$$

It is then convenient for compressible flows to recast the large-scale component in terms of a Favre-averaged variable

$$\tilde{f} = \overline{\rho f}/\bar{\rho} \tag{4}$$

With this formulation, the vector of dependent variables is given as

$$\boldsymbol{Q} = \frac{1}{J}\begin{bmatrix} \bar{\rho} \\ \bar{\rho}\tilde{u} \\ \bar{\rho}\tilde{v} \\ \bar{\rho}\tilde{w} \\ \bar{\rho}\tilde{E} \end{bmatrix} \tag{5}$$

and the vector fluxes by

$$\boldsymbol{F} = \frac{1}{J}\begin{bmatrix} \bar{\rho}\tilde{U} \\ \bar{\rho}\tilde{u}\tilde{U} + \xi_x \bar{p} \\ \bar{\rho}\tilde{v}\tilde{U} + \xi_y \bar{p} \\ \bar{\rho}\tilde{w}\tilde{U} + \xi_z \bar{p} \\ \bar{\rho}\tilde{E}\tilde{U} + \xi_{x_i} u_i \bar{p} \end{bmatrix} \tag{6}$$

$$\boldsymbol{G} = \frac{1}{J}\begin{bmatrix} \bar{\rho}\tilde{V} \\ \bar{\rho}\tilde{u}\tilde{V} + \eta_x \bar{p} \\ \bar{\rho}\tilde{v}\tilde{V} + \eta_y \bar{p} \\ \bar{\rho}\tilde{w}\tilde{V} + \eta_z \bar{p} \\ \bar{\rho}\tilde{E}\tilde{V} + \eta_{x_i} u_i \bar{p} \end{bmatrix} \tag{7}$$

$$\boldsymbol{H} = \frac{1}{J}\begin{bmatrix} \bar{\rho}\tilde{W} \\ \bar{\rho}\tilde{u}\tilde{W} + \zeta_x \bar{p} \\ \bar{\rho}\tilde{v}\tilde{W} + \zeta_y \bar{p} \\ \bar{\rho}\tilde{w}\tilde{W} + \zeta_z \bar{p} \\ \bar{\rho}\tilde{E}\tilde{W} + \zeta_{x_i} u_i \bar{p} \end{bmatrix} \tag{8}$$

$$\boldsymbol{F}_v = \frac{1}{J}\begin{bmatrix} 0 \\ \xi_{x_i}(\tilde{\sigma}_{i1} + \tau_{i1}) \\ \xi_{x_i}(\tilde{\sigma}_{i2} + \tau_{i2}) \\ \xi_{x_i}(\tilde{\sigma}_{i3} + \tau_{i3}) \\ \xi_{x_i}[\tilde{u}_j(\tilde{\sigma}_{ij} + \tau_{ij}) - \tilde{q}_i - \mathcal{Q}_i] \end{bmatrix} \tag{9}$$

$$\boldsymbol{G}_v = \frac{1}{J}\begin{bmatrix} 0 \\ \eta_{x_i}(\tilde{\sigma}_{i1} + \tau_{i1}) \\ \eta_{x_i}(\tilde{\sigma}_{i2} + \tau_{i2}) \\ \eta_{x_i}(\tilde{\sigma}_{i3} + \tau_{i3}) \\ \eta_{x_i}[\tilde{u}_j(\tilde{\sigma}_{ij} + \tau_{ij}) - \tilde{q}_i - \mathcal{Q}_i] \end{bmatrix} \tag{10}$$

$$\boldsymbol{H}_v = \frac{1}{J}\begin{bmatrix} 0 \\ \zeta_{x_i}(\tilde{\sigma}_{i1} + \tau_{i1}) \\ \zeta_{x_i}(\tilde{\sigma}_{i2} + \tau_{i2}) \\ \zeta_{x_i}(\tilde{\sigma}_{i3} + \tau_{i3}) \\ \zeta_{x_i}[\tilde{u}_j(\tilde{\sigma}_{ij} + \tau_{ij}) - \tilde{q}_i - \mathcal{Q}_i] \end{bmatrix} \tag{11}$$

where

$$\tilde{U} = \xi_t + \xi_{x_i}\tilde{u}_i \tag{12}$$

$$\tilde{V} = \eta_t + \eta_{x_i}\tilde{u}_i \tag{13}$$

$$\tilde{W} = \zeta_t + \zeta_{x_i}\tilde{u}_i \tag{14}$$

$$\tilde{E} = \tilde{T}\big/(\gamma - 1)M_r^2 + \tfrac{1}{2}(\tilde{u}^2 + \tilde{v}^2 + \tilde{w}^2) \tag{15}$$

In the preceding expressions, $\tilde{u}$, $\tilde{v}$, and $\tilde{w}$ are the Cartesian velocity components, $\bar{\rho}$ is the density, $\bar{p}$ is the pressure, and $\tilde{T}$ is the temperature. All length scales have been nondimensionalized by a representative distance l_r, and dependent variables have been normalized by their reference values except for $\bar{p}$, which has been nondimensionalized by $\rho_r u_r^2$. Components of the stress tensor and heat flux vector may be expressed as

$$\tilde{\sigma}_{ij} = \tilde{\mu}\left(\frac{\partial\xi_k}{\partial x_j}\frac{\partial\tilde{u}_i}{\partial\xi_k} + \frac{\partial\xi_k}{\partial x_i}\frac{\partial\tilde{u}_j}{\partial\xi_k} - \frac{2}{3}\delta_{ij}\frac{\partial\xi_l}{\partial x_k}\frac{\partial\tilde{u}_k}{\partial\xi_l}\right) \tag{16}$$

$$\tilde{\boldsymbol{q}}_i = -\left[\frac{1}{(\gamma - 1)M_r^2}\right]\left(\frac{\tilde{\mu}}{Pr}\right)\frac{\partial\xi_j}{\partial x_i}\frac{\partial\tilde{T}}{\partial\xi_j} \tag{17}$$

whereas the corresponding SGS stress and heat flux are provided by

$$\tau_{ij} = -Re\bar{\rho}(\widetilde{u_i u_j} - \tilde{u}_i\tilde{u}_j) \tag{18}$$

$$\mathcal{Q}_i = Re\bar{\rho}(\widetilde{u_i T} - \tilde{u}_i\tilde{T}) \tag{19}$$

For DNS, all variables may be replaced by their unfiltered forms and τ_{ij} and $\mathcal{Q}_i$ vanish, whereas for large-eddy computations, τ_{ij} and $\mathcal{Q}_i$ are obtained from the SGS model.

The Sutherland law for the molecular viscosity coefficient $\tilde{\mu}$ and the perfect gas relationship

$$\bar{p} = \bar{\rho}\tilde{T}\big/\gamma M_r^2 \tag{20}$$

are also employed, as is the Stokes hypothesis for the bulk viscosity coefficient.

Smagorinsky SGS Model

The first subgrid stress model was developed for incompressible flows by Smagorinsky,[20] based on the assumption that the turbulent kinetic energy production of the small-scale structures is balanced by dissipation. The compressible version of the model in trace-free form is given as

$$\mu_t = ReC\Delta^2\bar{\rho}\tilde{\mathcal{S}}_M \tag{21}$$

where

$$\tilde{\mathcal{S}}_M = (2\tilde{\mathcal{S}}_{ij}\tilde{\mathcal{S}}_{ij})^{\frac{1}{2}} \tag{22}$$

is the magnitude of the rate-of-strain tensor, and

$$\tilde{\mathcal{S}}_{ij} = \frac{1}{2}\left(\frac{\partial\xi_k}{\partial x_j}\frac{\partial\tilde{u}_i}{\partial\xi_k} + \frac{\partial\xi_k}{\partial x_i}\frac{\partial\tilde{u}_j}{\partial\xi_k}\right) \tag{23}$$

The eddy-viscosity length scale is taken as

$$\Delta = (1/J)^{\frac{1}{3}} \tag{24}$$

which corresponds to the width of the grid filtering function $\mathcal{G}$ in physical space, C is the eddy-viscosity model constant, and

$$\tau_{ij} - \tfrac{1}{3}\tau_{kk}\delta_{ij} = -2\mu_t\big(\tilde{\mathcal{S}}_{ij} - \tfrac{1}{3}\tilde{\mathcal{S}}_{kk}\delta_{ij}\big) \tag{25}$$

The isotropic part of the stress tensor, $\frac{1}{3}\tau_{kk}$, may be absorbed into an effective pressure for low-Mach-number flows, and the model degenerates to the original Smagorinsky form. For compressible applications, this term is accounted for according to Yoshizawa[21] as

$$\tau_{kk} = 2C_I\Delta^2\bar{\rho}\tilde{\mathcal{S}}_M^2 \tag{26}$$

To complete closure of the model, the SGS heat flux vector is specified in terms of a constant turbulent Prandtl number as

$$\mathcal{Q}_i = -\left(\frac{\mu_t}{Pr_t}\right)\frac{\partial\xi_j}{\partial x_i}\frac{\partial\tilde{T}}{\partial\xi_j} \tag{27}$$

The original Smagorinsky constant was given by $C_S = \sqrt{C}$. In near-wall regions, C_S must be multiplied by the van Driest damping factor

$$1 - \exp(n^+/A^+) \tag{28}$$

for the eddy viscosity to attain a more correct limiting behavior, where n^+ is the normal distance from the solid surface in law-of-the-wall coordinates and A^+ is the van Driest constant.

Dynamic SGS Model

The dynamic SGS model was first proposed by Germano et al.[4] for incompressible flows and extended by Moin et al.[22] for compressible applications. Its general formulation is identical to that of Smagorinsky[20] and Yoshizawa[21] given by Eqs. (21–27). In this description, however, the model constants C and C_I are computed as a function of time and space from the energy content of the resolved large-scale structures. This is accomplished by introducing a test filter function $\hat{\mathcal{G}}$, with a filter width that is wider than the computational mesh, where its application is represented as

$$\hat{f} = \int_{\mathcal{V}}\hat{\mathcal{G}}f\,\mathrm{d}\mathcal{V} \tag{29}$$

Differences between the subtest-scale stress and the SGS stress are then used to obtain values for the model constants. Details of the derivation may be found in Refs. 4, 22, and 23, which result in

$$C\Delta^2 = \frac{\big\langle\big(\mathcal{L}_{ij} - \frac{1}{3}\mathcal{L}_{kk}\delta_{ij}\big)\mathcal{M}_{ij}\big\rangle}{\langle\mathcal{M}_{ij}\mathcal{M}_{ij}\rangle} \tag{30}$$

where

$$\mathcal{L}_{ij} = \widehat{\bar{\rho}\tilde{u}_i\tilde{u}_j} - (1/\hat{\bar{\rho}})\widehat{\bar{\rho}\tilde{u}_i}\,\widehat{\bar{\rho}\tilde{u}_j} \tag{31}$$

$$\mathcal{M}_{ij} = -2(\hat{\Delta}/\Delta)^2\hat{\bar{\rho}}\hat{\tilde{\mathcal{S}}}_M\big(\hat{\tilde{\mathcal{S}}}_{ij} - \tfrac{1}{3}\hat{\tilde{\mathcal{S}}}_{kk}\delta_{ij}\big) + \widehat{2\bar{\rho}\tilde{\mathcal{S}}_M\big(\tilde{\mathcal{S}}_{ij} - \tfrac{1}{3}\tilde{\mathcal{S}}_{kk}\delta_{ij}\big)} \tag{32}$$

The normal stress constant is given by

$$C_I\Delta^2 = \langle\mathcal{L}_{kk}\rangle\big/\big\langle 2(\hat{\Delta}/\Delta)^2\hat{\bar{\rho}}\hat{\tilde{\mathcal{S}}}_M^2 - \widehat{2\bar{\rho}\tilde{\mathcal{S}}_M^2}\big\rangle \tag{33}$$

For the preceding expressions, the quantities enclosed by angle brackets $\langle\ \rangle$ indicate that a spatial average is to be performed along directions in which a particular flow may be homogeneous. This averaging process is introduced to regularize the distribution of the model coefficients, whose construction is highly ill conditioned.

When extended to the heat flux vector, the analysis also allows the turbulent Prandtl number to be determined as

$$Pr_t = C\Delta^2\frac{\langle\mathcal{N}_i\mathcal{N}_i\rangle}{\langle-\mathcal{K}_i\mathcal{N}_i\rangle} \tag{34}$$

where

$$\mathcal{K}_i = \widehat{\bar{\rho}\tilde{u}_i\tilde{T}} - (1/\hat{\bar{\rho}})\widehat{\bar{\rho}\tilde{u}_i}\,\widehat{\bar{\rho}\tilde{T}} \tag{35}$$

$$\mathcal{N}_i = (\hat{\Delta}/\Delta)^2 \hat{\bar{\rho}} \hat{\tilde{\mathcal{S}}}_M \frac{\partial \xi_j}{\partial x_i} \frac{\partial \hat{\tilde{T}}}{\partial \xi_j} - \widehat{\bar{\rho} \tilde{\mathcal{S}}_M \frac{\partial \xi_j}{\partial x_i} \frac{\partial \tilde{T}}{\partial \xi_j}} \tag{36}$$

The only adjustable parameter inherent in the model is the ratio of the test-filter width to the grid-filter width, $\hat{\Delta}/\Delta$. For all of the computations presented here, this ratio is taken as 2.0, which is consistent with the formulation of Germano et al.[4]

Numerical Method

Time-accurate solutions to Eq. (1) were obtained numerically by the implicit approximately factored finite difference algorithm of Beam and Warming[24] employing Newton-like subiterations (see Ref. 25), which has evolved as an efficient tool for generating solutions to a wide variety of complex fluid flow problems and which may be represented notationally as follows:

$$\begin{aligned}
&\left[I + \left(\frac{2\Delta t}{3}\right)\delta_{\xi 2}\left(\frac{\partial \boldsymbol{F}^p}{\partial \boldsymbol{Q}} - \frac{1}{Re}\frac{\partial \boldsymbol{F}_v^p}{\partial \boldsymbol{Q}}\right)\right] \\
&\quad \times \left[I + \left(\frac{2\Delta t}{3}\right)\delta_{\eta 2}\left(\frac{\partial \boldsymbol{G}^p}{\partial \boldsymbol{Q}} - \frac{1}{Re}\frac{\partial \boldsymbol{G}_v^p}{\partial \boldsymbol{Q}}\right)\right] \\
&\quad \times \left[I + \left(\frac{2\Delta t}{3}\right)\delta_{\zeta 2}\left(\frac{\partial \boldsymbol{H}^p}{\partial \boldsymbol{Q}} - \frac{1}{Re}\frac{\partial \boldsymbol{H}_v^p}{\partial \boldsymbol{Q}}\right)\right]\Delta \boldsymbol{Q} = -\left(\frac{2\Delta t}{3}\right) \\
&\quad \times \left[\left(\frac{1}{2\Delta t}\right)(3\boldsymbol{Q}^p - 4\boldsymbol{Q}^n + \boldsymbol{Q}^{n-1}) + \delta_{\xi 6}\left(\boldsymbol{F}^p - \frac{1}{Re}\boldsymbol{F}_v^p\right)\right. \\
&\quad \left. + \delta_{\eta 6}\left(\boldsymbol{G}^p - \frac{1}{Re}\boldsymbol{G}_v^p\right) + \delta_{\zeta 6}\left(\boldsymbol{H}^p - \frac{1}{Re}\boldsymbol{H}_v^p\right)\right]
\end{aligned} \tag{37}$$

In this expression, which was employed to advance the solution in time, $\boldsymbol{Q}^{p+1}$ is the $p+1$ approximation to $\boldsymbol{Q}$ at the $n+1$ time level $\boldsymbol{Q}^{n+1}$, and $\Delta\boldsymbol{Q} = \boldsymbol{Q}^{p+1} - \boldsymbol{Q}^p$. For $p = 1$, $\boldsymbol{Q}^p = \boldsymbol{Q}^n$. Second-order-accurate, backward-implicit time differencing has been used to represent temporal derivatives.

The implicit segment of the algorithm incorporated second-order-accurate centered differencing for all spatial derivatives and utilized nonlinear artificial dissipation[26] to augment stability. Efficiency was enhanced by solving this implicit portion of the factorized equations in diagonalized form.[27] Temporal accuracy, which can be degraded by use of the diagonal form, is maintained by utilizing subiterations within a time step. This technique has been commonly invoked to reduce errors due to factorization, linearization, and explicit application of boundary conditions. It is useful for achieving temporal accuracy on overset zonal mesh systems and for a domain decomposition implementation on parallel computing platforms. Any deterioration of the solution caused by use of artificial dissipation and by lower-order spatial resolution of implicit operators is also reduced by the procedure. Three subiterations per time step have been applied for the computations presented here. This treatment has been shown to provide acceptable levels of temporal accuracy for the computation of a convecting vortex[28] and the DNS of a forced transitional wall jet.[29]

The compact difference scheme employed on the right-hand side of Eq. (37) is based on the pentadiagonal system of Lele[30] and is capable of attaining spectrallike resolution. This is achieved through the use of a centered implicit difference operator with a compact stencil, thereby reducing the associated discretization error. The sixth-order tridiagonal subset of Lele's system is illustrated here in one spatial dimension as

$$\alpha\left(\frac{\partial f}{\partial \xi}\right)_{i-1} + \left(\frac{\partial f}{\partial \xi}\right)_i + \alpha\left(\frac{\partial f}{\partial \xi}\right)_{i+1} = a\left(\frac{f_{i+1} - f_{i-1}}{2}\right) + b\left(\frac{f_{i+2} - f_{i-2}}{4}\right) \tag{38}$$

with

$$\alpha = \tfrac{1}{3}, \qquad a = \tfrac{14}{9}, \qquad b = \tfrac{1}{9} \tag{39}$$

The scheme has been adapted by Visbal and Gaitonde[28] as an implicit iterative time-marching technique, applicable for unsteady vortical flows. It is used in conjunction with a 10th-order nondispersive spatial filter developed by Gaitonde et al.,[31] which has been applied after every subiteration in the present computations and which has been shown to be superior to the use of explicitly added artificial dissipation for maintaining both stability and accuracy on stretched curvilinear meshes.[28]

Repeated application of the spatial filter can result in shock waves that are excessively diffuse. This deficiency is overcome by replacing the compact-differencing of convective derivatives and use of filtering, by Roe's upwind-biased scheme,[32] using the MUSCL approach[33] with van Leer's harmonic limiter,[34] locally in regions of shock waves. The switch of Swanson and Turkel,[35] which is based on the second difference of pressure, is used as a sensor to determine where these regions occur.

In the computations that follow, the test filter incorporated for the dynamic subgrid stress model was formulated as a one-dimensional seven-point explicit centered stencil in each coordinate direction. Coefficients of the stencil were obtained by performing a least-squares curve fit of the filter transfer function to that of a sharp-cutoff filter, where the filter width was approximately twice that of the 10th-order spatial filter that was employed for solution of the flow equations. Spatial derivatives that must be evaluated for the computation of $\tilde{\mathcal{S}}_M$ were approximated by fourth-order explicit stencils, and the dynamic SGS model constants were numerically restricted such that

$$C \geq 0.0, \qquad C_I \geq 0.0, \qquad Pr_t \geq 0.2 \tag{40}$$

This restriction was required because certain quantities, appearing in the denominator of the expressions used to evaluate the model coefficients, vanished in the inviscid regions of the flowfield.

The aforementioned features of the numerical algorithm are embodied in an existing fully vectorized time-accurate three-dimensional computer code, FDL3DI,[36] which has proven to be reliable for steady and unsteady fluid flow problems, including the simulation of flows over delta wings with leading-edge vortices,[37–40] vortex breakdown,[38–40] DNS of transitional wall jets[29] and synthetic jet actuators,[41] and DNS and LES of subsonic channel and cylinder flowfields.[19]

Results

Reference conditions for the computations considered here are $l_r = 2.41 \times 10^{-4}$ m, $M_r = 3.0$, $Re = 6.5 \times 10^3$, and $Re_\theta = 1.696 \times 10^3$. In the results that follow, large-scale variables were decomposed into time-mean values and fluctuating components as, for example,

$$\tilde{u} = u_m + u' \tag{41}$$

The reference velocity u_r was taken as the freestream value, and for Smagorinsky[20] LES computations the following parameters were specified:

$$C_S = 0.065, \qquad C_I = 0.0066, \qquad A^+ = 25.0 \tag{42}$$

For the purpose of comparison, computations were performed in which no explicit subgrid-stress model was employed. Because it could not be established that all important structures were adequately resolved in such calculations, these are not referred to as DNS. They may, however, be considered to correspond to LES, whereby the characteristics of the numerical scheme provide an implicit SGS model. This technique has commonly been referred to as monotonically integrated LES.[42,43] In the present applications, this implicit dependence is accounted for by the high-order nondispersive spatial filter.

Compression-ramp solutions were generated at conditions corresponding to the DNS of Adams[17,18] for the Mach 3.0 flow past an 18-deg corner. In Adams's computations, the Reynolds number based on freestream quantities and the mean momentum thickness of the incoming boundary layer was 1685, and the computational domain was discretized with 1.44×10^7 grid points. An analysis of the solution indicated that the flowfield was "sufficiently well resolved."[18] Although a small region of mean separated flow developed about the corner, no large-scale shock wave motion was detected.

For the present simulations, a computational domain size was taken to be similar to that of Adams,[17,18] which is given in terms of the mean incoming boundary-layer thickness δ_0 as

$$L_x = 28.1\delta_0, \qquad L_y = 4.7\delta_0, \qquad L_z = 2.9\delta_0 \tag{43}$$

where L_x, L_y, and L_z are streamwise, vertical, and spanwise extents, respectively. The vertical extent L_y corresponds to the domain height at the inflow location. Grid spacing is uniform in the streamwise direction, except in the region near the corner. Beyond the streamwise extent L_x noted in Eq. (43), rapid stretching of the streamwise mesh to the outflow boundary was employed to provide a nonreflective buffer zone. In the vertical direction at the inflow boundary, geometric stretching of the y grid lines was utilized, with a constant mesh spacing ratio of 1.017.

A two-dimensional grid was elliptically generated in an x–y plane using automated software[44] to maintain orthogonality between grid lines. The two-dimensional grid was then uniformly distributed along the span, where constant spacing and a five grid plane overlap at domain boundaries was employed. Dimensions of the grids for these computations appear in Table 1. At the inflow location, the grid had the following minimum spacings in wall units:

$$\Delta x^+ = 15.1, \qquad \Delta y^+ = 1.4, \qquad \Delta z^+ = 8.3 \tag{44}$$

Based on the mean incoming profile, 79 of the 151 vertical grid points were within the boundary layer.

Inflow data for the compression-ramp simulations were obtained from a spatially evolving flat-plate DNS, which was used to generate profiles similar to those of Adams.[17,18] This computation itself required a separate DNS to effect transition on the plate. A schematic representation of the process is given in Fig. 1. The procedure consisted of employing a temporal half-channel DNS centered at the plate inflow boundary, with symmetry conditions enforced at the top of the domain, and an artificial source term introduced as a driving mechanism to mimic an imposed zero pressure gradient, thereby maintaining a fixed mass-flow rate.[19] Periodic conditions were specified in the streamwise direction, which had an extent of $10\delta_0$. After perturbing the half-channel flowfield, it was allowed to evolve temporally to a fully turbulent state, and fluctuating data at the streamwise center location were recorded.

The flat-plate computational domain was initialized with a compressible Blasius profile, where the boundary-layer thickness was approximately $\delta_0/3$ to allow for streamwise growth. Because the recorded half-channel DNS profiles were unlike those of a boundary layer, only the fluctuating components were retained. These were then rescaled in the vertical direction to match the Blasius profile thickness and used as perturbations to the flat-plate inflow. Transition occurred in a short distance downstream from inflow. The simulation was allowed to proceed sufficiently long so that reliable mean flowfield information could be collected. The streamwise location at which Reynolds number Re_θ most closely matched that of Adams[17,18] was determined, and instantaneous values for all dependent variables were extracted.

As was done by Adams[17,18] to reduce computational expense, instantaneous values were recorded for a nondimensional period $t = 70\delta_0$. The data were then made periodic by fitting a Fourier series to each variable at every grid point on the inflow boundary. A total of 2267 samples (one per time step) were collected, which were approximated by 600 terms in the series. The resultant inflow data could then be recycled into the compression-ramp domain for computational times greater than $t = 70\delta_0$. This procedure, which is essentially identical to that of Adams,[17,18] avoids artificial forcing of the boundary layer at a frequency below its characteristic value and ensures that the inflow data are sufficiently decorrelated before they are recycled.[18]

Because the vertical and spanwise grids for the half-channel, flat-plate, and compression-ramp inflow domains are identical, no spatial interpolation of the solutions was required. A comparison of the mean incoming boundary-layer parameters with those of Adams[45] is found in Table 2. Although the momentum thickness θ_0 closely matched Adams's value, the displacement δ_0^* was considerably smaller due differences in the streamwise velocity profile. This is demonstrated by the mean streamwise velocity profiles in Fig. 2. The present result resembles that of a fully developed equilibrium turbulent boundary layer, whereas those of Adams seem to be transitional. In addition, although fluctuating quantities were qualitatively similar to those of Adams, their magnitudes were somewhat higher. Also presented in Fig. 2 are fluctuating streamwise velocity profiles. Once again, the current profile is representative of a fully turbulent boundary layer.

For all simulations, including those used to generate inflow data, the time step was specified as $\Delta t = 0.1$. A preliminary solution employing no subgrid model was obtained on a coarse computational mesh and interpolated to the nominal grid. Flowfields for each computation were then initialized with this basic solution. Every case was then allowed to evolve for one period of the cycled inflow profiles (2267 time steps) to attain a turbulent equilibrium state. This corresponded approximately to 2.5 flow times through the streamwise extent L_x noted in Eq. (43). Solutions then continued to evolve for an additional 5.5 periods of the inflow data, corresponding to

Table 1 Compression-ramp flow grids

Reference	Grid size
Present	$(421 \times 151 \times 81)$
Adams[17,18]	$(1000 \times 180 \times 80)$

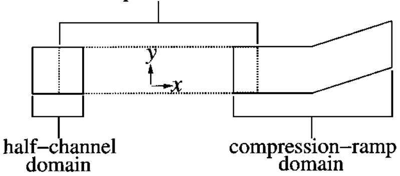

Fig. 1 Schematic of computational domains used to generate inflow profiles.

Table 2 Mean incoming boundary-layer parameters

Reference	δ_0	θ_0	δ_0^*	C_{f0}	$Re_{\theta0}$
Present	3.202	0.261	0.834	2.634×10^{-3}	1696
Adams[45]	3.239	0.259	1.381	2.651×10^{-3}	1685

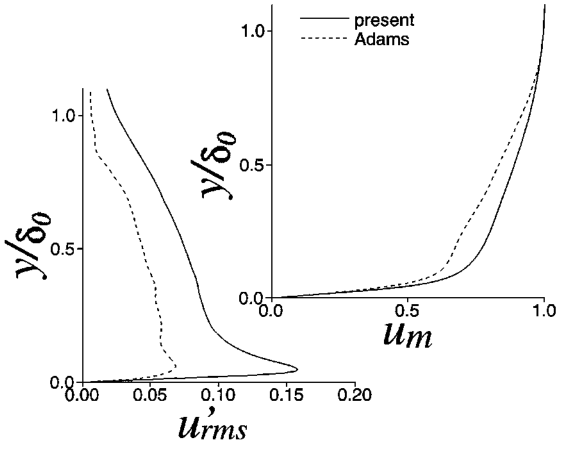

Fig. 2 Spanwise-averaged mean and fluctuating streamwise velocity profiles for inflow.

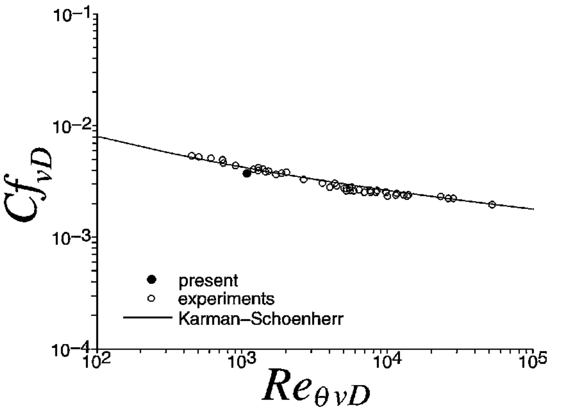

Fig. 3 Spanwise-averaged mean skin-friction correlation for flow upstream of the corner.

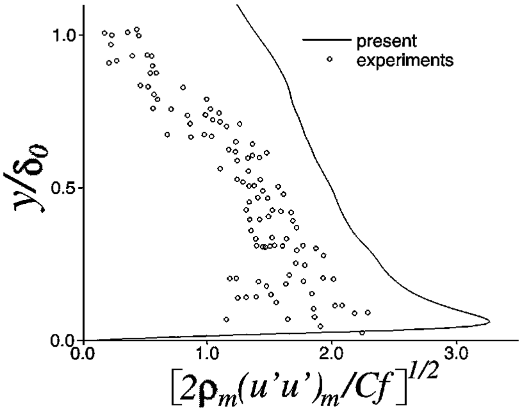

Fig. 4 Spanwise-averaged fluctuating streamwise velocity profiles for flow upstream of the corner.

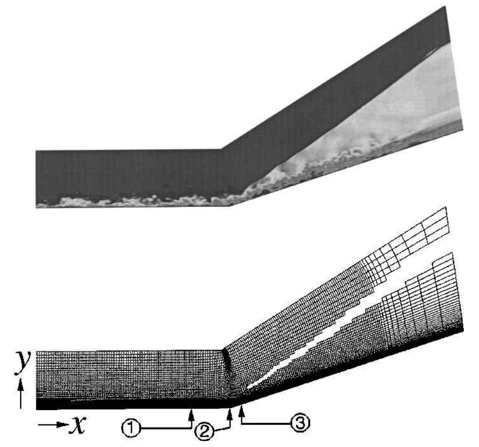

Fig. 5 Typical instantaneous Mach number contours for the no-model case at the midspan location and computational grid in an x–y plane indicating shock-capturing stencils and solution comparison stations.

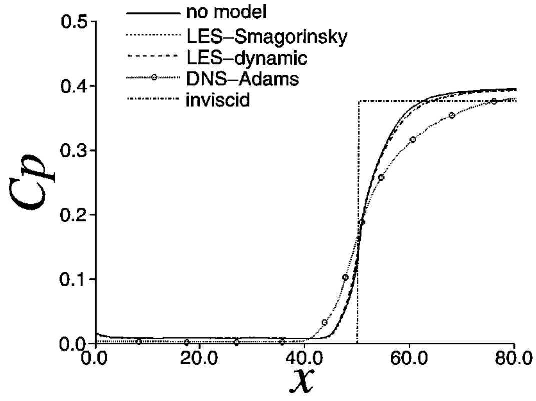

Fig. 6 Spanwise-averaged mean surface pressure coefficient distributions.

12,469 time steps and 13.9 flow-through times, over which statistical information was recorded.

At the inflow boundary, instantaneous values obtained by the aforementioned procedure were prescribed for all dependent variables. Simple extrapolation was employed at the outflow plane downstream of the stretched-mesh region. On the solid surface, the no-slip condition was enforced together with a fourth-order-accurate representation of zero normal pressure gradient. The isothermal temperature $T = 2.522$ was also specified along this surface, corresponding to the condition of Adams.[17,18] Because the top of the computational domain was located above the shock, simple extrapolation was applied along the upper boundary. At the spanwise ends of the domain, periodicity was implemented using the overlapping grid planes.

Shown in Fig. 3 are the flat plate skin-friction coefficient correlations of Hopkins and Inouye.[46] Here, both Cf and Reynolds number Re_θ have been corrected for compressibility according to the van Driest II (see Ref. 46) scaling. Experimental data collected for $1.5 \leq M_\infty \leq 5.8$, along with the empirical relationship of Karman and Schoenherr (see Ref. 46) are indicated. The present time-mean spanwise-averaged result, taken from the flat-plate region upstream of the interaction, compares well with the other correlations.

Seen in Fig. 4 is a profile of the spanwise-averaged fluctuating streamwise velocity component, also taken at a location on the flat-plate portion of the flowfield ahead of the interaction. Here the velocity intensity has been normalized by the wall stress. The experimental data in Fig. 4 are those appearing in Ref. 47, which correspond to a number of measurements taken at $1.72 \leq M_\infty \leq 4.67$. The present fluctuations are somewhat larger than the data, which were all collected at a considerably higher Reynolds number.

Typical instantaneous results of the no model compression-ramp flowfield solution at the midspan location are found in Fig. 5. Mach number contours are provided in the upper portion of Fig. 5, whereas the grid structure is indicated in the lower portion. Areas of the grid that are blanked out correspond to mesh points where convective derivatives are obtained via the Roe upwind-biased scheme. In Fig. 5, only every other i grid and every third j grid line are displayed. It is evident that the upwind-biased evaluation is confined locally to a small region surrounding the shock wave, so that accuracy of the high-order method is not compromised in other regions of the flowfield. Also seen in Fig. 5 are streamwise locations where profile data will be compared to the solution of Adams,[17,18] which are labeled as 1, 2, and 3, respectively.

Spanwise-averaged time-mean surface pressure coefficient distributions from the current simulations are presented in Fig. 6, along with the DNS of Adams.[45] All of the present computations are seen to be in close agreement with each other, but differ considerably from Adams's result. The overall pressure rise is greater than the inviscid value due to the displacement effect of the boundary layer, which is appreciable at the low Reynolds number considered here. Corresponding skin-friction coefficient distributions appear in Fig. 7. It is noted that the solution of Adams[45] predicts a more extensive region of separation, as well as a greater rise downstream. The disparity between the respective results is attributed to the differences in the incoming profiles.

Although no measurements are available at the flow conditions of the compression-ramp simulations, it is useful to compare the numerical results to experimental data that were taken at higher Reynolds numbers. The investigations of Smits and Muck[8] and those of Settles et al.[13] examined flows past compression ramps of varying angles. Table 3 indicates the conditions for these experiments. Measured and computed surface pressure distributions are shown in Fig. 8. Here, the streamwise coordinate x has been normalized by δ_0, and its origin has been translated to the ramp corner, as was done in Ref. 13. In addition, the pressure coefficient

Table 3 Comparison of flow conditions

Reference	M_r	$Re_{\delta 0}$	Ramp angle, deg
Present	3.0	2.1×10^4	18
Adams[17,18]	3.0	2.1×10^4	18
Smits and Muck[8]	2.9	1.6×10^6	16, 20
Settles et al.[13]	2.85	1.7×10^6	16, 20

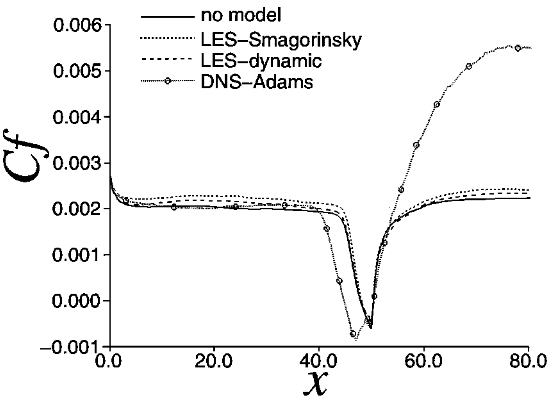

Fig. 7 Spanwise-averaged mean skin-friction coefficient distributions.

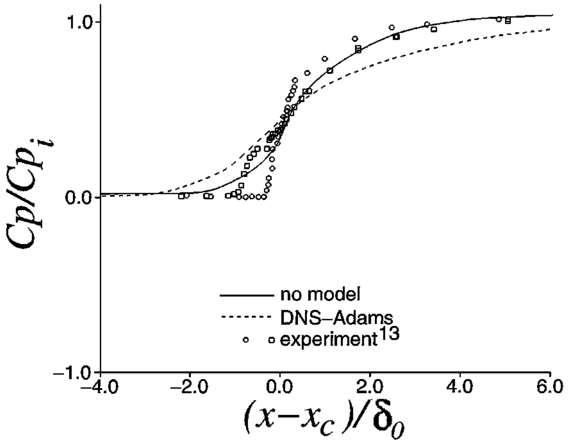

Fig. 8 Spanwise-averaged mean surface pressure coefficient distributions.

was normalized by that of the inviscid pressure rise C_{pi} to collapse the data from all ramp angles to a more universal form. The current pressure distribution correlates well with the experiments, particularly downstream of the corner. Corresponding skin-friction distributions are shown in Fig. 9. Because the experiments were conducted at much higher Reynolds numbers than the computations, the skin-friction coefficient has been normalized by its value upstream of the interaction C_{f1}, to bring the distributions to similar levels. The 16-deg compression-ramp flow is unseparated. Greater regions of reversed flow occur in the computations than in the 20-deg ramp experiments due to the low Reynolds number. In the recovery region downstream of reattachment, the present solution is similar to that of Settles et al.,[13] whereas that of Adams[17,18] compares favorably with the data of Smits and Muck.[8]

Found in Fig. 10 are mean streamwise velocity profiles in terms of the van Driest velocity[48] normalized by the friction velocity and plotted in law-of-the-wall units at stations 1 and 3. Station 2 is not shown in Fig. 10 because the flow is separated at that location, and the friction velocity is, therefore, ill formulated. Upstream of separation at station 1, the solutions compare well with the linear and logarithmic profiles. This is not true downstream at station 3 because the flow has not attained equilibrium following the interaction. Mean profiles of the streamwise velocity component are also provided in Fig. 11. It is observed that present solutions are in close agreement with each other, but differ from the solution of Adams.[45]

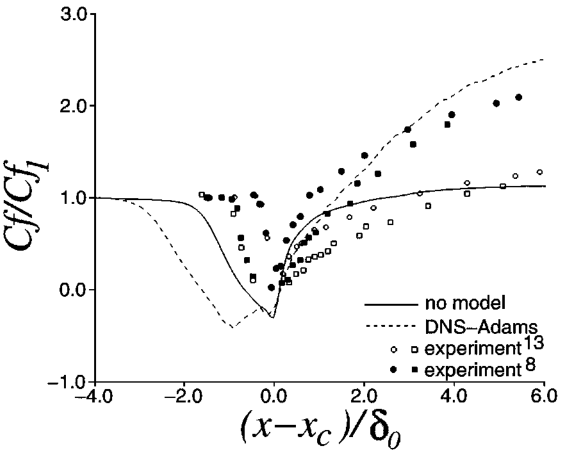

Fig. 9 Spanwise-averaged mean skin-friction coefficient distributions.

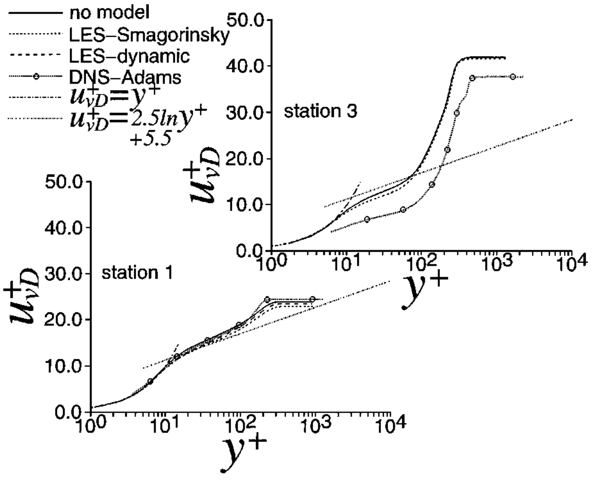

Fig. 10 Spanwise-averaged mean streamwise velocity profiles in the near-wall region.

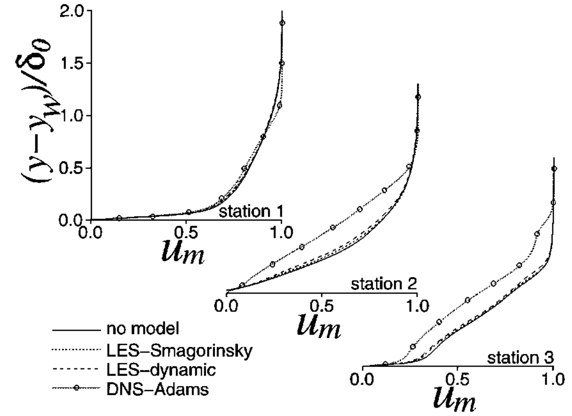

Fig. 11 Spanwise-averaged mean streamwise velocity profiles.

The qualitative behavior of Adams's solution is much like the present simulations, except that the profiles have been displaced away from the wall because of the more extensive separated flow region. Mean temperature profiles are shown in Fig. 12. In this case, the present solutions are not similar to Adams's result, for which aerodynamic heating of the wall occurs at stations 2 and 3.

Fluctuating streamwise velocity components are presented in Fig. 13. At station 1, the profiles may be compared with those of the inflow in Fig. 2. It is evident that the present solutions have changed little from their inflow states, whereas that of Adams has evolved to a more fully turbulent condition. At downstream stations 2 and 3, the current results are qualitatively similar to those of Adams, except

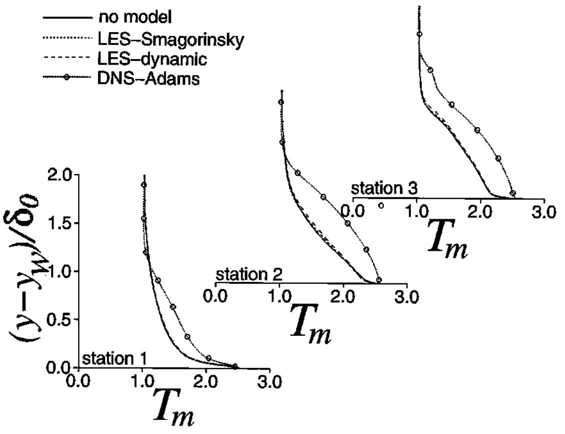

Fig. 12 Spanwise-averaged mean temperature profiles.

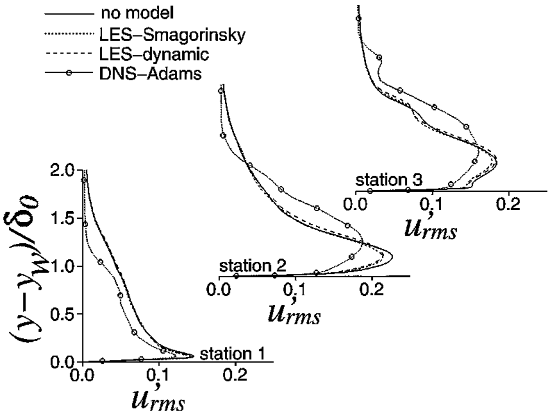

Fig. 13 Spanwise-averaged fluctuating streamwise velocity profiles.

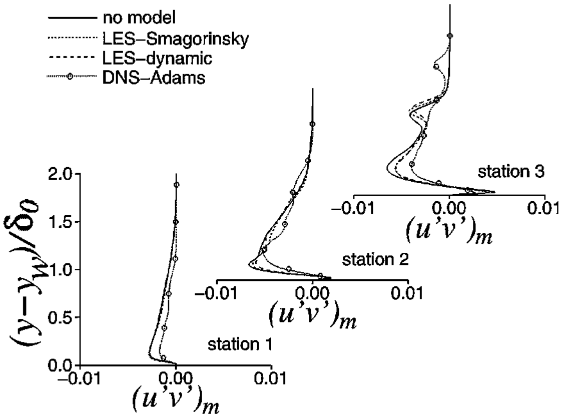

Fig. 14 Spanwise-averaged Reynolds shear stress profiles.

for the earlier noted displacement. A secondary peak observed in u' at station 3 is associated with the location of the shock wave in the mean flowfield. Reynolds stress profiles are compared in Fig. 14, where it is noted that the present solutions have magnitudes that are generally greater than those of Adams.[45] Fluctuating temperatures are seen in Fig. 15. As was true for the mean temperature profiles, the present results are quite different from those of Adams. All fluctuating quantities in Figs. 13–15 show an expected amplification downstream of the shock.

Spanwise turbulent energy spectra at specific x and y locations appear in Fig. 16. These locations at stations 1, 2, and 3 lie along a constant vertical grid index rather than at a constant distance

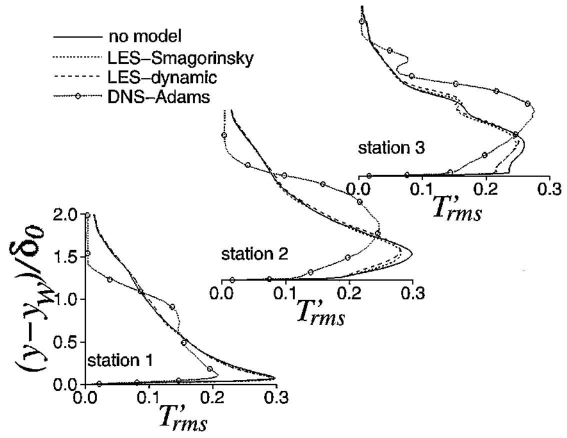

Fig. 15 Spanwise-averaged fluctuating temperature profiles.

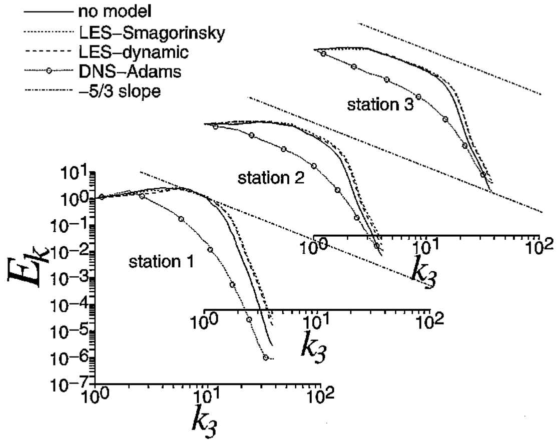

Fig. 16 Spanwise turbulent kinetic energy spectra.

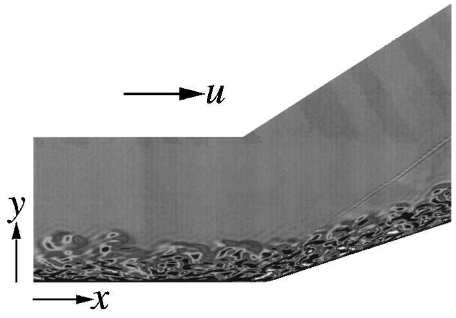

Fig. 17 Instantaneous Ω_z contours for the no-model case at the midspan location.

from the wall. At the inflow boundary, this index has the following location:

$$y^+ = 7.3, \qquad y/\delta_0 = 0.034 \tag{45}$$

Instantaneous spectra have been temporally averaged in Fig. 16, and E_k, has been normalized by its value at $k_3 = 1$. The present results are consistently higher than those of Adams,[45] indicating a greater level of turbulent kinetic energy present in the flowfield.

Because of the extensive computational resources required to perform these simulations, a comprehensive grid resolution study could not be performed. Although there exists no concept of grid independence for LES,[49] it is beneficial to carry out coarse-grid computations for the purpose of determining their suitability for practical applications. Toward this end, LESs were generated on a coarser grid than that employed here. A description of these computations, along with other results, may be found in Ref. 50.

Some features of the compression-ramp flowfield are shown in Figs. 17 and 18. Instantaneous contours of the spanwise component

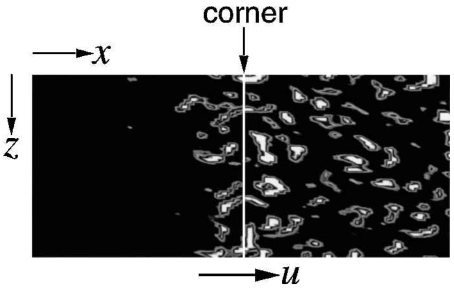

Fig. 18 Instantaneous Ω_z contours for the no-model case at $y^+ = 10.39$.

of vorticity from the no-model case are shown in Fig. 17. Fine-scale structures of the turbulent boundary layer can be observed in Fig. 17. Similar contours are presented in Fig. 18. In this case, however, the view is from above the solid surface, looking down toward the wall. The surface of the contours corresponds to a fixed vertical grid location, which at the inflow boundary is situated at a distance above the wall of $y^+ = 10.39$. An increase in vorticity downstream of the corner due to the shock interaction is clearly observed.

Summary

A high-order compact difference scheme was used to perform LESs for the Mach 3.0 flow past an 18-deg compression ramp. Both the Smagorinsky[20] and dynamic[4] subgrid stress models were considered in the computations, along with a simulation in which no model was employed.

Solutions compared favorably with experimental data taken at much higher Reynolds numbers and with the previous computation of Adams.[17,18] Because of differences in the inflow profiles between the present and previous simulations, which could not be matched, it was expected that variations in the resultant solutions would occur. The hybrid numerical method, which employed a Roe upwind-biased scheme locally in the vicinity of shock waves, and the high-order scheme elsewhere, was found to be an effective technique for capturing the shock while maintaining accuracy in smooth regions of the flowfield. This technique, therefore, appears promising as a means performing DNS and LES of flowfields containing strong shock waves.

LESs appeared relatively insensitive to the exact form of the subgrid stress model employed. For the mean flowfield, the maximum value of the eddy-viscosity coefficient μ_t evolving from the simulations was 4.4 for the dynamic model[4] and 9.0 for the Smagorinsky[20] model. These maximums occurred in the region near the foot of the shock wave. Similarly to the solution of Adams,[17,18] no large-scale shock-wave motion was observed.

Acknowledgments

The work presented here was sponsored by the U.S. Air Force Office of Scientific Research under Task 2307 AW and was monitored by L. Sakell. Computational resources were supported in part by a grant of supercomputer time from the U.S. Department of Defense Major Shared Resource Centers at Wright–Patterson Air Force Base, Ohio; Vicksburg, Mississippi; Stennis Space Center, Mississippi; and Aberdeen Proving Ground, Maryland. The authors are grateful to N. A. Adams for furnishing details of his investigation, for his assistance in supplying us with results of his computations, and for numerous general discussions.

References

[1] Ristorcelli, J. R., and Blaisdell, G. A., "Consistent Initial Conditions for the DNS of Compressible Turbulence," *Physics of Fluids A*, Vol. 9, No. 1, 1997, pp. 4–6.

[2] Rai, M. M., Gatski, T. B., and Erlebacher, G., "Direct Simulation of Spatially Evolving Compressible Turbulent Boundary Layers," AIAA Paper 95-0583, Jan. 1995.

[3] Spyropoulos, E. T., and Blaisdell, G. A., "Large-Eddy Simulation of a Spatially Evolving Supersonic Turbulent Boundary-Layer Flow," *AIAA Journal*, Vol. 36, No. 11, 1998, pp. 1983–1990.

[4] Germano, M., Piomelli, U., Moin, P., and Cabot, W. H., "A Dynamic Subgrid-Scale Eddy Viscosity Model," *Physics of Fluids A*, Vol. 3, No. 7, 1991, pp. 1760–1765.

[5] Lee, S., Lele, S. V., and Moin, P., "Direct Numerical Simulation of Isotropic Turbulence Interacting with a Weak Shock Wave," *Journal of Fluid Mechanics*, Vol. 251, June 1993, pp. 533–562.

[6] Ducros, F., Ferrand, V., Nicoud, F., Weber, C., Darracq, D., Gacherieu, C., and Poinsot, T., "Large-Eddy Simulation of the Shock/Turbulence Interaction," *Journal of Computational Physics*, Vol. 152, No. 2, 1999, pp. 517–549.

[7] Andreopoulos, J., and Muck, K. C., "Some New Aspects of the Shock-Wave/Boundary-Layer Interaction in Compression-Ramp Flows," *Journal of Fluid Mechanics*, Vol. 180, July 1987, pp. 405–428.

[8] Smits, A. J., and Muck, K.-C., "Experimental Study of Three Shock Wave/Turbulent Boundary Layer Interactions," *Journal of Fluid Mechanics*, Vol. 182, Sept. 1987, pp. 291–314.

[9] Dolling, D. S., and Murphy, M. T., "Unsteadiness of the Separation Shock Wave Structure in a Supersonic Compression Ramp Flowfield," *AIAA Journal*, Vol. 23, No. 12, 1983, pp. 1628–1634.

[10] Dolling, D. S., and Or, C. T., "Unsteadiness of the Shock Wave Structure in Attached and Separated Compression Ramp Flows," *Experiments in Fluids*, Vol. 3, No. 1, 1985, pp. 24–32.

[11] Erengil, E. E., and Dolling, D. S., "Unsteady Wave Structure Near Separation in a Mach 5 Compression Ramp Interaction," *AIAA Journal*, Vol. 29, No. 5, 1990, pp. 728–735.

[12] Erengil, M. E., and Dolling, D. S., "Correlation of Separation Shock Motion with Pressure Fluctuations in the Incoming Boundary Layer," *AIAA Journal*, Vol. 29, No. 11, 1991, pp. 1868–1877.

[13] Settles, G. S., Fitzpatrick, T. J., and Bogdonoff, S. M., "Detailed Study of Attached and Separated Compression Corner Flowfields in High Reynolds Number Supersonic Flow," *AIAA Journal*, Vol. 17, No. 6, 1979, pp. 579–585.

[14] Hunt, D., and Nixon, D., "A Very Large-Eddy Simulation of an Unsteady Shock-Wave/Turbulent Boundary-Layer Interaction," AIAA Paper 95-2212, June 1995.

[15] Urbin, G., Knight, D., and Zheltovodov, A. A., "Compressible Large-Eddy Simulation using Unstructured Grid: Supersonic Turbulent Boundary Layer and Compression Corner," AIAA Paper 99-0427, Jan. 1999.

[16] Urbin, G., Knight, D., and Zheltovodov, A. A., "Large-Eddy Simulation of a Supersonic Compression Corner Part I," AIAA Paper 2000-0398, Jan. 2000.

[17] Adams, N. A., "Direct Numerical Simulation of Turbulent Compression Ramp Flow," *Theoretical and Computational Fluid Dynamics*, Vol. 12, No. 2, 1998, pp. 109–129.

[18] Adams, N. A., "Direct Simulation of the Turbulent Boundary Layer along a Compression Ramp at $M = 3$ and $Re_\theta = 1685$," *Journal of Fluid Mechanics*, Vol. 420, Oct. 2000, pp. 47–83.

[19] Rizzetta, D. P., Visbal, M. R., and Blaisdell, G. A., "Application of a High-Order Compact Difference Scheme to Large-Eddy and Direct Numerical Simulation," AIAA Paper 99-3714, June 1999.

[20] Smagorinsky, J. S., "General Circulation Experiments with the Primitive Equations," *Monthly Weather Review*, Vol. 91, No. 3, 1963, pp. 99–165.

[21] Yoshizawa, A., "Statistical Theory for Compressible Turbulent Shear Flows, with the Application to Subgrid Modeling," *Physics of Fluids*, Vol. 29, No. 7, 1986, pp. 2152–2164.

[22] Moin, P., Squires W., Cabot, W., and Lee, S., "A Dynamic Subgrid-Scale Model for Compressible Turbulence and Scalar Transport," *Physics of Fluids A*, Vol. 3, No. 11, 1991, pp. 2746–2757.

[23] Lilly, D. K., "A Proposed Modification of the Germano Subgrid-Scale Closure Method," *Physics of Fluids A*, Vol. 4, No. 3, 1992, pp. 633–635.

[24] Beam, R., and Warming, R., "An Implicit Factored Scheme for the Compressible Navier–Stokes Equations," *AIAA Journal*, Vol. 16, No. 4, 1978, pp. 393–402.

[25] Gordnier, R. E., and Visbal, M. R., "Numerical Simulation of Delta-Wing Roll," AIAA Paper 93-0554, Jan. 1993.

[26] Jameson, A., Schmidt, W., and Turkel, E., "Numerical Solutions of the Euler Equations by Finite Volume Methods Using Runge–Kutta Time Stepping Schemes," AIAA Paper 81-1259, June 1981.

[27] Pulliam, T. H., and Chaussee, D. S., "A Diagonal Form of an Implicit Approximate-Factorization Algorithm," *Journal of Computational Physics*, Vol. 39, No. 2, 1981, pp. 347–363.

[28] Visbal, M. R., and Gaitonde, D. V., "High-Order-Accurate Methods for Complex Unsteady Subsonic Flows," *AIAA Journal*, Vol. 37, No. 10, 1999, pp. 1231–1239.

[29] Visbal, M., Gaitonde, D., and Gogineni, S., "Direct Numerical Simulation of a Forced Transitional Plane Wall Jet," AIAA Paper 98-2643, June 1998.

[30] Lele, S. A., "Compact Finite Difference Schemes with Spectral-Like Resolution," *Journal of Computational Physics*, Vol. 103, No. 1, 1992, pp. 16–42.

[31] Gaitonde, D., Shang, J. S., and Young, J. L., "Practical Aspects of High-Order Accurate Finite-Volume Schemes for Electromagnetics," AIAA Paper 97-0363, Jan. 1997.

[32] Roe, P. L., “Approximate Riemann Solvers, Parameter Vectors and Difference Schemes,” *Journal of Computational Physics*, Vol. 43, No. 2, 1981, pp. 357–372.

[33] van Leer, B., “Flux-Vector Splitting for the Euler Equations,” Inst. for Computer Applications in Science and Engineering, ICASE Rept. 82-30, Hampton, VA, Sept. 1982.

[34] van Leer, B., “Towards the Ultimate Conservation Difference Scheme. V. A Second-Order Sequel to Godunov’s Method,” *Journal of Computational Physics*, Vol. 32, No. 1, 1979, pp. 101–136.

[35] Swanson, R. C., and Turkel, E., “On Central-Differencing and Upwind Schemes,” *Journal of Computational Physics*, Vol. 101, No. 2, 1992, pp. 292–306.

[36] Gaitonde, D., and Visbal, M. R., “High-Order Schemes for Navier–Stokes Equations: Algorithm and Implementation into FDL3DI,” U.S. Air Force Research Lab., AFRL-VA-WP-TR-1998-3060, Wright–Patterson AFB, OH, Aug. 1998.

[37] Gordnier, R. E., and Visbal, M. R., “Numerical Simulation of Delta-Wing Roll,” *Aerospace Science and Technology*, Vol. 2, No. 6, 1998, pp. 347–357.

[38] Gordnier, R. E., “Computation of Delta-Wing Roll Maneuvers,” *Journal of Aircraft*, Vol. 32, No. 3, 1995, pp. 486–492.

[39] Visbal, M. R., “Computational Study of Vortex Breakdown on a Pitching Delta Wing,” AIAA Paper 93-2974, July 1993.

[40] Visbal, M. R., “Onset of Vortex Breakdown Above a Pitching Delta Wing,” *AIAA Journal*, Vol. 32, No. 8, 1994, pp. 1568–1575.

[41] Rizzetta, D. P., Visbal, M. R., and Stanek, M. J., “Numerical Investigation of Synthetic-Jet Flowfields,” *AIAA Journal*, Vol. 37, No. 8, 1999, pp. 919–927.

[42] Boris, J. P., Grinstein, F. F., Oran, E. S., and Kolbe, R. J., “New Insights into Large Eddy Simulation,” *Fluid Dynamic Research*, Vol. 10, No. 4–6, 1992, pp. 199–227.

[43] Fureby, C., and Grinstein, F. F., “Monotonically Integrated Large-Eddy Simulation,” *AIAA Journal*, Vol. 37, No. 5, 1999, pp. 544–556.

[44] Steinbrenner, J. P., Chawner, J. P., and Fouts, C. L., “The GRIDGEN 3D Multiple Block Grid Generation System, Volume II: User’s Manual,” Wright Research and Development Center, WRDC-TR-90-3022, Feb. 1991.

[45] Adams, N. A., “DNS Data for the Turbulent Boundary Layer Along a Compression Ramp at $M = 3$ and $Re = 1685$,” [online database], URL: http://www.ifd.mavt.ethz.ch/database/dns/cc.3.18.1685/Docu.htm [cited 20 Dec. 1999].

[46] Hopkins, E. J., and Inouye, M., “An Evaluation of Theories for Predicting Skin Friction and Heat Transfer on Flat Plates at Supersonic and Hypersonic Mach Numbers,” *AIAA Journal*, Vol. 9, No. 6, 1971, pp. 993–1003.

[47] Smits, A. J., and Dussauge, J.-P., *Turbulent Shear Layers in Supersonic Flow*, American Inst. of Physics, Woodbury, NY, 1996, p. 13.

[48] van Driest, E. R., “On the Turbulent Flow near a Wall,” *Journal of the Aeronautical Sciences*, Vol. 23, No. 11, 1956, pp. 1007–1011.

[49] Ghosal, S., “Mathematical and Physical Constraints on Large-Eddy Simulation of Turbulence,” *AIAA Journal*, Vol. 37, No. 4, 1999, pp. 425–433.

[50] Rizzetta, D. P., Visbal, M. R., and Gaitonde, D. V., “Direct Numerical and Large-Eddy Simulation of Supersonic Flows by a High-Order Method,” AIAA Paper 2000-2408, June 2000.

J. Kallinderis
Associate Editor